On Robot Localization Safety for Fixed-Lag Smoothing: Quantifying the Risk of Misassociation

Osama Abdul Hafez[1], Guillermo Duenas Arana[1], Yihe Chen[1], Mathieu Joerger[2], and Matthew Spenko[1]

Abstract— **Monitoring localization safety will be necessary to certify the performance of robots that operate in life-critical applications, such as autonomous passenger vehicles or delivery drones because many current localization safety methods do not account for the risk of undetected sensor faults. One type of fault, misassociation, occurs when a feature extracted from a mapped landmark is associated to a non-corresponding landmark and is a common source of error in feature-based navigation applications. This paper accounts for the probability of misassociation when quantifying landmark-based mobile robot localization safety for fixed-lag smoothing estimators. We derive a mobile robot localization safety bound and evaluate it using simulations and experimental data in an urban environment. Results show that localization safety suffers when landmark density is relatively low such that there are not enough landmarks to adequately localize and when landmark density is relatively high because of the high risk of feature misassociation.**

I. Introduction

There have been significant advancements in self-driving vehicles resulting in an impressive number of autonomously driven miles on public roads [1]. However, miles driven are insufficient to prove safety— strong statistical evidence of safety would require billions of miles all while assuming that the on-board algorithms and sensors have not changed during testing [2]. Simulations can help, but they might not account for intricate real-world edge-cases [3]. Instead, more rigorous, analytical approaches can and must be used used to assess autonomous vehicle performance. As such, this paper investigates the safety assessment of one subsystem in autonomous vehicles: *localization*. More specifically, this paper is the first to introduce the impact of misassociation faults on the localization safety of landmark-based fixed lag smoothing estimator. Misassociation event occurs when a feature extracted from a mapped landmark is associated to a non-corresponding landmark, which is a common source of failure in feature-based navigation applications.

In robotics, most pose estimation research has focused on improving the quality of batch and sequential localization and mapping [4], [5], [6], [7], [8]. Only a few papers assessed pose estimation safety, and they either utilized a particle spread or covariance envelope [9], [10], [11], which are insufficient because they do not account for measurement faults [12]. Measurement faults are unknown deterministic errors that cannot be modeled using a zero-mean Gaussian distribution. Examples include excessive Global Navigation Satellite Systems (GNSS) clock errors, misassociations among mapped objects, unmapped static objects mistaken as parts of the map, and measurements due to dynamic objects. If such faults are not detected, they might result in large pose estimate errors with hazardous consequences.

There is some prior work on identifying such faults by testing discrepancy among measurements [13], [14], [15], but such approaches do not provide any statistical proofs on the detection performance. Instead, this paper employs a more appropriate metric to assess pose estimation safety, localization *integrity* [16]. Specifically, integrity risk is the probability that the pose estimation error will exceed an allowable tolerance level without warning the system.

For decades, integrity risk has been the main safety metric for open-sky GNSS aviation applications [17], [18], [19]. Lately, integrity monitoring techniques have been extended to mobile robots in GNSS degraded environments. For example, [20] develops an integrity monitoring-based fault detection and isolation mechanism for fused lidar and GPS measurements with an Unscented Kalman Filter estimator. A novel approach to build protection levels on estimate error for optimization-based visual localization has been proposed by [21]. Other work has performed integrity monitoring for lidar-based Extended Kalman Filter (EKF) localization by accounting for the risk of misassociation in global nearest neighbors [22] or local nearest neighbors [23] data association techniques. Such methods have been extended to account for unmapped objects associated to mapped landmarks using a solution-separation [24] or innovation-based approach [25]. The role of Inertial Measurement Units (IMUs) in reducing misassociation risk has been studied in [26], and using integrity risk in a model predictive control framework to generate a safe trajectory has been investigated in [27].

All of the aforementioned research upper-bounds the integrity risk given a wrong association by one. To obtain a tighter bound, [28] developed an Extended Kalman Filter (EKF)-based integrity monitor that can handle measurement faults sequentially from the prior estimate to the current estimate under the worst case scenario, which has been extended in [29], [30] to account for the risk of incorrect association and to handle measurement faults sequentially within a preceding time window to improve the tightness of the bound.

These methods focused on landmark-based localization via EKFs while [31] developed a method to monitor integrity offline using fixed lag smoothing for localization and a chi-squared residual for fault detection. Unlike EKFs, where a robot's current state is estimated using the current measurement and the prior pose estimate, fixed-lag smoothing

estimates a robot's pose over a preceding time window by employing all measurements received within this window *and* the prior pose estimate at the beginning of the window. Fixed-lag smoothing is considered by many a more robust estimator against linearization errors as compared to EKFs.

Quantifying localization integrity risk via fixed lag smoothing using a solution separation fault detector has been demonstrated and compared to the chi-squared residual approach by [32]. Prior work on fixed lag smoothing-based integrity monitoring assumed that the probability of failure for each feature is known a priori, but this is not accurate. To account for its variability, this paper extends the previous work to account for the risk of misassociations in the local nearest neighbor criterion under the impact of previous and current measurement faults.

The remainder of the paper begins with background on localization via fixed-lag smoothing where measurements may be affected by unknown deterministic errors (or what is referred to as *measurement faults*), a point that distinguishes this work from others. Section III defines the hazardous misleading information event. The estimate error and the fault detector distributions as well as the upper-bound on the conditional integrity risk for each fault hypothesis are derived in Section IV. Section V presents the probability of each fault hypothesis as a function of the measurement failure probabilities and provides a practical integrity monitor. The data association failure probability for each feature extracted from range measurements is derived in Section VI. Section VII assesses the method's performance using simulation and experimental data. Finally, conclusions and future work are presented in Section VIII.

II. FIXED-LAG SMOOTHING

This section presents the primary components of landmark-based localization via fixed-lag smoothing. First, the general non-linear optimization problem is described. Then, measurement models are expressed into a generalized form that allows us to leverage prior work in integrity monitoring for GNSS applications. Subsequently, the sensitivity of robot's pose estimate error to measurement errors is analyzed. The local nearest neighbor data association criterion, used to associate measurements extracted from sensors (e.g. lidar or camera) with landmarks in the map, for a fixed-lag smoothing estimator is then illustrated. Last, the use of chi-squared residual metric as a means of fault detection is described.

A. Problem Formulation

Robot pose estimation using fixed-lag smoothing is accomplished by determining the robot state at each epoch within a preceding time window of size M (including the current epoch) that minimizes the squared norm of the measurements' weighted residual:

$$\hat{\mathbf{x}}_{k,M} = \underset{\mathbf{x}_{k,M}}{\operatorname{argmin}} \sum_{i=1}^{n_{k,M}} \left\| \mathbf{z}_i - \mathbf{h}_i\left(\mathbf{x}_{k,M}\right) \right\|_{\mathbf{V}_i^{-1}}^2 \qquad (1)$$

where $\mathbf{z}_i \in \mathbb{R}^{n_i}$ is the ith measurement in the preceding time window with n_i being the number of features in the ith measurement, $\mathbf{x}_{k,M} = \begin{bmatrix} \mathbf{x}_{k-M}^T & \dots & \mathbf{x}_{k-1}^T & \mathbf{x}_k^T \end{bmatrix}^T$ is a vector of robot pose within the time window, such that $\mathbf{x}_k \in \mathbb{R}^m$ refers to the

state at the current time, $n_{k,M}$ is the number of measurements received within the time window, and $\|\mathbf{v}\|_{\mathbf{V}^{-1}}^2 = \mathbf{v}^T\mathbf{V}^{-1}\mathbf{v}$ is the norm squared of vector $\mathbf{v}$ weighted by $\mathbf{V}^{-1}$. Each of the measurements can be expressed as a non-linear function of the robot pose with additive noise and a possible fault:

$$\mathbf{z}_i = \mathbf{h}_i\left(\mathbf{x}_{k,M}\right) + \mathbf{v}_i + \mathbf{f}_i \qquad (2)$$

where $\mathbf{v}_i \sim \mathbb{N}\left(\mathbf{0}, \mathbf{V}_i\right)$ is the ith measurement's Gaussian white noise with $\mathbf{V}_i$ being the associated noise covariance matrix, $\mathbf{h}_i(\cdot)$ is the observation function of ith measurement, and $\mathbf{f}_i$ is the fault in the ith measurement, such that $\mathbf{f}_i$ is a vector of zeros if the ith measurement is non-faulted. This formulation can handle measurements that contain colored noise, by augmenting the dynamic model of the noise as an additional state [33].

Measurement faults are defined as rarely occurring unknown deterministic errors that do not obey the Gaussian white noise assumption and thus might result in a non-zero mean of the estimate error. The next subsection defines the different types of measurement models used in mobile robotics and reformulates them to match the general measurement model in (2).

B. Measurement Modeling

Absolute measurements, such as extracted features from lidar measurements or GNSS measurements, can be expressed in the form of (2). In landmark-based navigation, $\mathbf{h}_i(\cdot)$ relates robot pose to an extracted landmark's feature, $\mathbf{z}_i$ represents a feature's measurements extracted from a detected landmark, and $\mathbf{f}_i$ is a nonzero vector only when the detected landmark's feature measurements are faulted, e.g. associating a feature extracted from a mapped landmark to a non-corresponding landmark or associating an extracted feature from a moving or unmapped static object to a landmark in the map [23], [25]. A special case of absolute measurements that reflects the sequential impact of prior state estimate errors on the current robot pose estimate is the *prior measurement*, $\hat{\mathbf{x}}_{k-M} \in \mathbb{R}^m$, which represents the prior estimate of robot pose at the last epoch in the time window (or what is referred to as *pseudo measurements*):

$$\underbrace{\hat{\mathbf{x}}_{k-M}}_{\mathbf{z}_i} = \underbrace{\mathbf{x}_{k-M}}_{\mathbf{h}_i(\mathbf{x}_{k,M})} + \underbrace{\boldsymbol{\varepsilon}_{k-M}}_{\mathbf{v}_i} + \underbrace{\mathbf{f}_{k-M}}_{\mathbf{f}_i} \qquad (3)$$

where $\boldsymbol{\varepsilon}_{k-M} \sim \mathbb{N}\left(\mathbf{0}, \boldsymbol{\Lambda}_{k-M}^{-1}\right)$ is Gaussian uncertainty in the prior robot pose estimate and $\boldsymbol{\Lambda}_{k-M}$ is its information matrix.

Relative measurements, such as those that may come from accelerometers, gyroscopes, or wheel encoders, are commonly modeled as:

$$\mathbf{x}_{k-q+1} = \mathbf{g}_i\left(\mathbf{x}_{k-q}, \mathbf{u}_i\right) - \mathbf{w}_i \quad, \forall q \in \{1, 2, ..., M\} \qquad (4)$$

where $\mathbf{g}_i(\cdot, \cdot)$ is the state evolution model of the ith relative measurement, $\mathbf{u}_i$ is the ith relative measurement, $\mathbf{w}_i \sim \mathbb{N}\left(\mathbf{0}, \mathbf{W}_i\right)$ is the Gaussian white process noise in the ith relative measurement with $\mathbf{W}_i$ as the associated process noise covariance matrix (in this case, $\mathbf{w}_i$ is the projection of the ith relative measurement noise on the state space). To fit the

format provided by (2), the relative measurement model in (4) is reformulated as follows:

$$\underbrace{\mathbf{0}}_{\mathbf{z}_i} = \underbrace{\mathbf{x}_{k-q+1} - \mathbf{g}_i\left(\mathbf{x}_{k-q}, \mathbf{u}_i\right)}_{\mathbf{h}_i(\mathbf{x}_{k,M})} + \underbrace{\mathbf{w}_i}_{\mathbf{v}_i} + \underbrace{\mathbf{0}}_{\mathbf{f}_i} \;, \forall q \in \{1, 2, ..., M\}$$

$$(5)$$

C. Pose Estimation

This section describes the robot pose estimation process. The minimization problem in (1) can be expressed in batch form as:

$$\hat{\mathbf{x}}_{k,M} = \underset{\mathbf{x}_{k,M}}{\operatorname{argmin}} \left\| \mathbf{z} - \mathbf{h}\left(\mathbf{x}_{k,M}\right) \right\|_{\mathbf{V}^{-1}}^2 \qquad (6)$$

where $\mathbf{z} \in \mathbb{R}^N$ is the measurement vector, $N = \sum_{i=1}^{n_{k,M}} n_i$ is the number of independent measurements obtained during the time window, and $\mathbf{V} \in \mathbb{R}^{N \times N}$ is a block matrix of measurement noise covariance matrices along its diagonal. The optimization problem is solved by recursively linearizing the measurement function, $\mathbf{h}\left(\mathbf{x}_{k,M}\right)$, for example by using the Gauss-Newton method. After the optimization process converges, the observation function, $\mathbf{h}\left(\mathbf{x}_{k,M}\right)$, is linearized around the best robot pose estimate $\mathbf{x}_{k,M}^*$ (obtained in the last iteration of the optimization):

$$\hat{\boldsymbol{\delta}}_{k,M} = \underset{\boldsymbol{\delta}_{k,M}^*}{\operatorname{argmin}} \left\| \mathbf{z} - \mathbf{h}\left(\mathbf{x}_{k,M}^*\right) - \mathbf{H}_{k,M}\boldsymbol{\delta}_{k,M}^* \right\|_{\mathbf{V}^{-1}}^2 \qquad (7)$$

where $\mathbf{H}_{k,M} = \left.\frac{\partial \mathbf{h}(\mathbf{x}_{k,M})}{\partial \mathbf{x}_{k,M}}\right|_{\mathbf{x}_{k,M}^*}$ is the Jacobian of the observation function and $\boldsymbol{\delta}_{k,M}^* = \mathbf{x}_{k,M} - \mathbf{x}_{k,M}^*$. By defining $\mathbf{b}_{k,M} = \mathbf{V}^{-\frac{1}{2}}\left(\mathbf{z} - \mathbf{h}\left(\mathbf{x}_{k,M}^*\right)\right)$ as the weighted residual vector and $\mathbf{A}_{k,M} = \mathbf{V}^{-\frac{1}{2}}\mathbf{H}_{k,M}$ as the standardized measurement matrix, the pose estimate over the preceding time window, in (7), can be written using a quadratic form:

$$\hat{\boldsymbol{\delta}}_{k,M} = \underset{\boldsymbol{\delta}_{k,M}^*}{\operatorname{argmin}} \left\| \mathbf{A}_{k,M}\boldsymbol{\delta}_{k,M}^* - \mathbf{b}_{k,M} \right\|^2 \qquad (8)$$

By utilizing the sparseness of the standardized measurement matrix, the minimization problem can be solved efficiently [34], [4]. The solution of the least squares problem in (8) is:

$$\hat{\boldsymbol{\delta}}_{k,M} = \boldsymbol{\Lambda}_{k,M}^{-1}\mathbf{A}_{k,M}^T\mathbf{b}_{k,M} \qquad (9)$$

where $\boldsymbol{\Lambda}_{k,M} = \mathbf{A}_{k,M}^T\mathbf{A}_{k,M}$ is the information matrix over the time window, $\hat{\boldsymbol{\delta}}_{k,M} = \hat{\mathbf{x}}_{k,M} - \mathbf{x}_{k,M}$ is the pose estimate error, and $\mathbf{x}_{k,M}$ is the true robot pose. The pose estimate error during the time window obtained using fixed-lag smoothing can be expressed as a function of measurement errors by substituting the definition of $\mathbf{b}_{k,M}$, after convergence, in (9):

$$\begin{aligned} \hat{\boldsymbol{\delta}}_{k,M} &= \boldsymbol{\Lambda}_{k,M}^{-1}\mathbf{A}_{k,M}^T\mathbf{V}^{-\frac{1}{2}}\left(\mathbf{z} - \mathbf{h}\left(\mathbf{x}_{k,M}\right)\right) \\ &= \boldsymbol{\Lambda}_{k,M}^{-1}\mathbf{A}_{k,M}^T\mathbf{V}^{-\frac{1}{2}}\left(\mathbf{v} + \mathbf{f}\right) \end{aligned} \qquad (10)$$

where $\mathbf{v} \in \mathbb{R}^N$ is the measurement noise vector, and $\mathbf{f} \in \mathbb{R}^N$ is the measurement fault vector.

D. Data Association

This section describes the local nearest neighbor data association criterion for fixed lag smoothing estimator. Since this work is tailored for landmark-based localization, the role of the data association algorithm is to associate feature measurements extracted from lidars or cameras to their corresponding landmarks in the pre-obtained map.

It is worth mentioning that this work uses t_l to designate landmark indices, whereas l to designate the feature of landmark t_l. In fixed lag smoothing localization, the individual residual vector, $\mathbf{b}_{k,M}^{j,t_l}$, between feature j and landmark t_l is used as a measure for data association, such that feature j is correctly associated if it is associated to $t_l = t_j$, which is defined as:

$$\mathbf{b}_{k,M}^{j,t_l} = \mathbf{V}_j^{-\frac{1}{2}}\left(\mathbf{z}_j - \mathbf{h}_{t_l}\left(\hat{\mathbf{x}}_{k,M}\right)\right) \qquad (11)$$

By expanding $\mathbf{z}_j$ and linearizing $\mathbf{h}_{t_l}\left(\hat{\mathbf{x}}_{k,M}\right)$ around $\mathbf{x}_{k,M}$, the individual residual vector, $\mathbf{b}_{k,M}^{j,t_l}$, would become:

$$\begin{aligned} \mathbf{b}_{k,M}^{j,t_l} &= \mathbf{V}_j^{-\frac{1}{2}}\left(\mathbf{h}_{t_j}\left(\mathbf{x}_{k,M}\right) + \mathbf{v}_j - \mathbf{H}_{k,M}^{t_l}\hat{\boldsymbol{\delta}}_{k,M} - \mathbf{h}_{t_l}\left(\mathbf{x}_{k,M}\right)\right) \\ &= \mathbf{V}_j^{-\frac{1}{2}}\left(\mathbf{y}_{k,M}^{t_j,t_l} + \mathbf{v}_j - \mathbf{H}_{k,M}^{t_l}\boldsymbol{\Lambda}_{k,M}^{-1}\mathbf{A}_{k,M}^T\mathbf{V}^{-\frac{1}{2}}\left(\mathbf{v} + \mathbf{f}\right)\right) \\ &= \mathbf{V}_j^{-\frac{1}{2}}\left(\mathbf{y}_{k,M}^{t_j,t_l} + \mathbf{v}_j\right) - \mathbf{A}_{k,M}^{t_l}\boldsymbol{\Lambda}_{k,M}^{-1}\mathbf{A}_{k,M}^T\mathbf{V}^{-\frac{1}{2}}\left(\mathbf{v} + \mathbf{f}\right) \end{aligned} \qquad (12)$$

where $\mathbf{y}_{k,M}^{t_j,t_l} = \mathbf{h}_{t_j}\left(\mathbf{x}_{k,M}\right) - \mathbf{h}_{t_l}\left(\mathbf{x}_{k,M}\right)$ is the relative separation between the landmark t_j (unknown) and landmark t_l (known) in the measurement space and $\mathbf{A}_{k,M}^{t_l} = \mathbf{V}_j^{-\frac{1}{2}}\mathbf{H}_{k,M}^{t_l}$ is the standardized observation matrix of the lth landmark. As a preliminary step to describe the local nearest neighbor data association criterion for fixed lag smoothing localization, the individual residual vector's distribution, $\mathbf{b}_{k,M}^{j,t_l}$, is defined as:

$$\mathbf{b}_{k,M}^{j,t_l} \sim \mathbb{N}\left(\mathbf{V}_j^{-\frac{1}{2}}\mathbf{y}_{k,M}^{t_j,t_l} - \mathbf{A}_{k,M}^{t_l}\boldsymbol{\Lambda}_{k,M}^{-1}\mathbf{A}_{k,M}^{t_l\,T}\mathbf{V}^{-\frac{1}{2}}\mathbf{f}, \mathbf{R}_{k,M}^{j,t_l}\right) \qquad (13)$$

where $\mathbb{N}(\mu, \Sigma)$ is a normal distribution with mean vector μ and covariance matrix Σ, and $\mathbf{R}_{k,M}^{j,t_l}$ is the individual residual vector's covariance matrix, which can be expressed as follows:

$$\mathbf{R}_{k,M}^{j,t_l} = \left(\mathbf{E}_j - \mathbf{A}_{k,M}^{t_l}\boldsymbol{\Lambda}_{k,M}^{-1}\mathbf{A}_{k,M}^T\right)\left(\mathbf{E}_j - \mathbf{A}_{k,M}^{t_l}\boldsymbol{\Lambda}_{k,M}^{-1}\mathbf{A}_{k,M}^T\right)^T \qquad (14)$$

such that $\mathbf{E}_j$ is the jth feature extraction matrix.

In landmark based fixed lag smoothing localization, the local nearest neighbor algorithm utilizes the individual residual vector, $\mathbf{b}_{k,M}^{j,t_l}$, to associate feature measurements with the corresponding landmarks in the map recursively within each iteration of the optimization until convergence. Specifically, it associates feature j to landmark t_* if it satisfies:

$$t_* = \underset{t_l}{\operatorname{argmin}} \; \left\| \mathbf{b}_{k,M}^{j,t_l} \right\|_{\mathbf{R}_{k,M}^{j,t_l}{}^{-1}} \quad \text{and} \quad \left\| \mathbf{b}_{k,M}^{j,t_*} \right\|_{\mathbf{R}_{k,M}^{j,t_*}{}^{-1}} < T^n \qquad (15)$$

where T^n is a predefined threshold that determines the validation region for each landmark.

308

E. Fault Detection

The fault detector, q_k, which checks whether the robot's operation can continue, is a statistical measure of estimation's measurement discrepancy that is used to trigger an alarm whenever it exceeds a predefined threshold, T_k, $q_k > T_k$. Here, the squared norm of the residual vector, or what is referred to as the chi-squared metric, is used as a fault detector:

$$q_k = \left\| \mathbf{V}^{-\frac{1}{2}} \left(\mathbf{z} - \mathbf{h} \left(\hat{\mathbf{x}}_{k,M} \right) \right) \right\|^2 \tag{16}$$

Accordingly, the chi-squared fault detector can be expressed as a function of measurement errors by substituting the definition of $\hat{\mathbf{x}}_{k,M} = \mathbf{x}_{k,M} + \hat{\boldsymbol{\delta}}_{k,M}$ in (16):

$$\begin{aligned} q_k &= \left\| \mathbf{V}^{-\frac{1}{2}} \left(\mathbf{v} + \mathbf{f} \right) - \mathbf{A}_{k,M} \hat{\boldsymbol{\delta}}_{k,M} \right\|^2 \\ &= \left\| \left(\mathbf{I} - \mathbf{A}_{k,M} \boldsymbol{\Lambda}_{k,M}^{-1} \mathbf{A}_{k,M}^T \right) \mathbf{V}^{-\frac{1}{2}} \left(\mathbf{v} + \mathbf{f} \right) \right\|^2 \end{aligned} \tag{17}$$

This section introduced fixed-lag smoothing localization, the associated local nearest neighbors data association criterion, and the chi-squared based fault detection mechanism. The next will define Hazardous Misleading Information.

III. HAZARDOUS MISLEADING INFORMATION

Localization safety is quantified as integrity risk, the probability of Hazardous Misleading Information (HMI), which occurs when the state-of-interest's estimate error, $\boldsymbol{\alpha} \in \mathbb{R}^{(M+1)m}$, (e.g. lateral error) surpasses an alert limit, l, and the fault detector, q_k, does not trigger an alarm [29]:

$$HMI_k = q_k \leq T_k \cap \left| \boldsymbol{\alpha}^T \hat{\boldsymbol{\delta}}_{k,M} \right| > l \tag{18}$$

where n_H is the number of fault hypotheses. The probability of HMI, $P(HMI)$, is evaluated under every fault hypothesis, $H_h, \forall i \in \{0,...,n_H\}$, where the fault hypothesis specifies which measurements are faulted and H_0 is the fault-free hypothesis.

Since the state-of-interest estimate error and fault detector are both influenced by measurement faults in the preceding time window, the set of hypotheses must account for measurement faults taking place within the time window. In robotics, fixed-lag smoothing is commonly utilized as a recursive estimator by including the prior estimate, $\hat{\mathbf{x}}_{k-M}$ (computed by fixed-lag smoothing in the previous epoch, $\hat{\mathbf{x}}_{k-1,M}$) as a measurement. Thus, the impact of measurement faults happening at epochs prior to the preceding time window must be considered by incorporating the possibility of having faults in the prior estimate among the set of hypotheses. In this work, the probability of having faults in the prior estimate is upper-bounded by one. Then, given a set of mutually exclusive, collectively exhaustive fault hypotheses, $\{H_0, \ldots, H_{n_H}\}$, the $P(HMI)$, or integrity risk, is quantified as follows:

$$P(HMI_k) = \sum_{h=0}^{n_H} P(HMI_k \mid H_h) P(H_h) \tag{19}$$

where $P(HMI_k \mid H_h)$ is the current conditional integrity risk given the hth fault hypothesis, and $P(H_h)$ is the probability of occurrence for the hth hypothesis.

The following sections will upper-bound the right hand side of (19) to obtain a conservative measure of localization safety. Next, $P(HMI_k \mid H_h)$ will be quantified.

IV. INTEGRITY MONITORING

This section upper-bounds the probability of HMI for a given fault hypothesis, $P(HMI_k \mid H_h)$. To quantify the conditional integrity risk, the statistical distribution of the state-of-interest estimate error, $\boldsymbol{\alpha}^T \hat{\boldsymbol{\delta}}_{k,M}$, and the fault detector, q_k, needs to be specified. First, from (10) and relying on the Gaussian white noise assumption of $\mathbf{v}$, the distribution of the state-of-interest estimate error, $\boldsymbol{\alpha}^T \hat{\boldsymbol{\delta}}_{k,M}$, is:

$$\boldsymbol{\alpha}^T \hat{\boldsymbol{\delta}}_{k,M} \sim \mathbb{N} \left(\boldsymbol{\alpha}^T \boldsymbol{\Lambda}_{k,M}^{-1} \mathbf{A}_{k,M}^T \mathbf{V}^{-\frac{1}{2}} \mathbf{f}, \boldsymbol{\alpha}^T \boldsymbol{\Lambda}_{k,M}^{-1} \boldsymbol{\alpha} \right) \tag{20}$$

where $\mathbb{N}(\mu, \Sigma)$ is a normal distribution with mean μ, and covariance matrix Σ. Second, from (17), and utilizing the fact that $\mathbf{V}^{-\frac{1}{2}} (\mathbf{v})$ is a vector of standard normal random variables and that $\left(\mathbf{I} - \mathbf{A}_{k,M} \boldsymbol{\Lambda}_{k,M}^{-1} \mathbf{A}_{k,M}^T \right)$ is an idempotent matrix, the distribution of the fault detector, q_k, is:

$$q_k \sim \chi_{n_{k,M} - (M+1)m, \lambda_k}^2 \tag{21}$$

where $\chi_{a,b}^2$ refers to a non-central chi-squared distribution with a degrees of freedom and non-centrality parameter b. The non-centrality parameter for q_k is:

$$\lambda_k = \mathbf{f}^T \mathbf{V}^{-\frac{1}{2}} \left(\mathbf{I} - \mathbf{A}_{k,M} \boldsymbol{\Lambda}_{k,M}^{-1} \mathbf{A}_{k,M}^T \right) \mathbf{V}^{-\frac{1}{2}} \mathbf{f} \tag{22}$$

The degrees of freedom is less than $n_{k,M}$ because the robot pose estimate, $\hat{\mathbf{x}}_{k,M}$, is linearly dependant on the measurement vector, $\mathbf{z}$. Moreover, given the distribution of q_k, the current detector's threshold, T_k, can be chosen to limit the risk of false alarms, or *continuity risk*, to a pre-allocated value, I_{FA}:

$$P(q_k > T_k | H_0) = I_{FA} \tag{23}$$

Accordingly, the fault detector's threshold, T_k is:

$$T_k = X_{n_{k,M} - (M+1)m}^{-2} [1 - I_{FA}] \tag{24}$$

where $X_b^{-2}[\cdot]$ is the inverse cumulative distribution function of the central chi-squared distribution with b degrees of freedom.

The conditional probability of HMI given the h_{th} fault hypothesis is defined as:

$$P(HMI_k \mid H_h) = P \left(q_k \leq T_k \cap \left| \boldsymbol{\alpha}^T \hat{\boldsymbol{\delta}}_{k,M} \right| > l \mid H_h \right) \tag{25}$$

The fact that the statistical distribution of the state-of-interest estimate error, $\boldsymbol{\alpha}^T \hat{\boldsymbol{\delta}}_{k,M}$, and the fault detector, q_k, are different, makes the evaluation of their joint probability complex. Fortunately, [35] proved that for batch estimators, the chi-squared detector is statistically independent from the pose estimate error. Thus, the conditional integrity risk can be expressed as:

$$P(HMI_k \mid H_h) = P(q_k \leq T_k \mid H_h) P \left(\left| \boldsymbol{\alpha}^T \hat{\boldsymbol{\delta}}_{k,M} \right| > l \mid H_h \right) \tag{26}$$

By utilizing the distributions of the fault detector, q_k, and the state-of-interest estimate error, $\boldsymbol{\alpha}^T \hat{\boldsymbol{\delta}}_{k,M}$, the conditional integrity risk, $P(HMI_k \mid H_h)$, is expanded as follows:

$$P(HMI_k \mid H_h) = \left(\Phi \left[\frac{l - \mu_{\boldsymbol{\alpha}^T \hat{\boldsymbol{\delta}}_k}}{\sqrt{\boldsymbol{\alpha}^T \boldsymbol{\Lambda}_{k,M}^{-1} \boldsymbol{\alpha}}} \right] \right.$$

$$\left. - \Phi \left[\frac{-l - \mu_{\boldsymbol{\alpha}^T \hat{\boldsymbol{\delta}}_k}}{\sqrt{\boldsymbol{\alpha}^T \boldsymbol{\Lambda}_{k,M}^{-1} \boldsymbol{\alpha}}} \right] \right) X_{n_{k,M}-(M+1)m,\lambda_k}^2 [T_k] \quad (27)$$

where $\Phi[\cdot]$ is the standard Gaussian Cumulative Distribution Function (CDF), $X_{a,b}^2$ is the chi-squared CDF with a degrees of freedom and non-centrality parameter b, $\mu_{\boldsymbol{\alpha}^T \hat{\boldsymbol{\delta}}_{k,M}}$ is the current estimate error's mean as defined in (20), and λ_k is the current detector's non-centrality parameter defined in (22). Note that $\mu_{\boldsymbol{\alpha}^T \hat{\boldsymbol{\delta}}_{k,M}}$ and λ_k are both influenced by measurement faults, $\mathbf{f}$.

Because the true measurement faults are unknown, quantifying $P(HMI_k \mid H_h)$ is upper-bounded by searching for the fault vector that maximizes it (the worst-case fault vector) given the set of faulted measurements in the hth hypothesis, H_h:

$$\mathbf{f}_h^{worst} = \mathbf{f}_h^{dir} \mathbf{f}_h^{mag} \quad (28)$$

where $\mathbf{f}_h^{dir}$ is the direction of the worst-case fault vector (unit vector), and $\mathbf{f}_h^{mag}$ is the magnitude of the worst-case fault vector (scalar). [35] showed that the worst-case fault vector's direction, $\mathbf{f}_h^{dir}$, can be quantified in a closed form as:

$$\mathbf{f}_h^{dir} = \mathbf{F}_h^T \left[\mathbf{F}_h \left(\mathbf{I} - \mathbf{A}_{k,M} \boldsymbol{\Lambda}_{k,M}^{-1} \mathbf{A}_{k,M}^T \right) \mathbf{F}_h^T \right]^{-1} \mathbf{F}_h \mathbf{A}_{k,M} \boldsymbol{\Lambda}_{k,M}^{-1} \boldsymbol{\alpha} \quad (29)$$

where $\mathbf{F}_h$ is the extraction matrix of the faulted measurements assumed by the hth hypothesis. After substituting $\mathbf{f}_h^{dir}$ in (27), the upper-bound on $P(HMI_k \mid H_h)$ is evaluated by searching for $\mathbf{f}_h^{mag}$, that maximizes (27).

$$P(HMI_k \mid H_h) \leq \max_{\mathbf{f}_h^{mag}} \left[\left(\Phi \left[\frac{l - \mu_{\boldsymbol{\alpha}^T \hat{\boldsymbol{\delta}}_{k,M}}}{\sqrt{\boldsymbol{\alpha}^T \boldsymbol{\Lambda}_{k,M}^{-1} \boldsymbol{\alpha}}} \right] \right. \right.$$

$$\left. \left. - \Phi \left[\frac{-l - \mu_{\boldsymbol{\alpha}^T \hat{\boldsymbol{\delta}}_{k,M}}}{\sqrt{\boldsymbol{\alpha}^T \boldsymbol{\Lambda}_{k,M}^{-1} \boldsymbol{\alpha}}} \right] \right) X_{n_{k,M}-(M+1)m,\lambda_k}^2 [T_k] \right] \quad (30)$$

This section derived an upper-bound on $P(HMI_k \mid H_h)$. Thus, the only remaining part to monitor integrity is to evaluate the probabilities of each fault hypotheses, $P(H_h)$, which is addressed in the following section.

V. FAULT HYPOTHESIS PROBABILITIES

This section evaluates the probability of occurrence for each fault hypothesis, $P(H_h)$. To do so, the individual probability of failure for each measurement, P_i, needs to be quantified, which can be done either theoretically or experimentally based on the nature and quality of each measurement. The quantification of these probabilities will be illustrated later in this paper.

Given the fault probability of every measurement within the preceding time window, the probability of hypothesis H_h with the set of faulted measurements $j = 1, \ldots, r$ is given as:

$$P(H_h) = P(H_0) \prod_{j=1}^{r} \frac{P_j}{1 - P_j} \quad (31)$$

where $P(H_0) = \prod_{i=1}^{n_{k,M}} 1 - P_i$ is the probability of fault-free hypothesis [36]. Note, this work assumes that measurement faults are statistically independent, i.e. given that one of the measurements is faulted, the fault probability of others does not change.

Monitoring integrity for all possible hypotheses can be computationally infeasible, even for a few number of measurements in the time window. Accordingly, this work upper-bounds the integrity risk by limiting the hypotheses to be monitored to the ones in which the number of simultaneous measurement faults in the time window is less than or equal to a specific number, n_{max}, while accounting for the risk of more than n_{max} simultaneous faults. Thus, the upper-bound on the integrity risk would become:

$$P(HMI_k) \leq I_{>n_{max}} + \sum_{\substack{h=0 \\ h \notin >n_{max}}}^{n_H} P(HMI_k \mid H_h) P(H_h) (1 - I_{>n_{max}}) \quad (32)$$

where $I_{>n_{max}}$ is the probability of more than n_{max} measurements to be faulted simultaneously, which can be upper-bounded as follows (see Appendix C of [36] for the proof):

$$I_{>n_{max}} \leq \frac{\left(\sum_{i=1}^{n_{k,M}} P_i \right)^{n_{max}+1}}{(n_{max}+1)!} \quad (33)$$

Since this work is focused on quantifying localization safety for landmark based navigation, the next section will assess the risk of failure for measurements extracted from feature-based sensors, e.g. lidars or cameras.

VI. DATA ASSOCIATION FAILURE PROBABILITY

This section upper-bounds the failure probability of features extracted from lidar or camera measurements. There are two modes in which the features can fail. First, the Mis-Association (MA) event: a feature extracted from a mapped landmark is associated to a non-corresponding landmark in the map. Second, the Unmapped Association (UA) event: a feature corresponding to a moving or unmapped static object is associated to a landmark in the map. Thus, the probability of failure for any associated feature, j, can be expressed as:

$$P_j = P(UA_j \cup MA_j) \quad (34)$$

Due to the fact that the unmapped association and mis-association events cannot occur simultaneously for a specific feature, equation (34) can be written as follows:

$$P_j = P(UA_j) + P(MA_j) \quad (35)$$

The probability of unmapped association is assumed to be a constant that can be assessed using limited experimentation.

This work focuses on quantifying the risk of mis-association for localization via fixed-lag smoothing. Based on fixed lag smoothing-based local nearest neighbors criterion illustrated

in (15), the probability of mis-association for feature j is:

$$P(MA_j) = P\left(\bigcup_{\substack{t_r \\ t_r \neq t_j}} \left[\|\mathbf{b}_{k,M}^{j,t_r}\|_{\mathbf{R}_{j,t_r}^{-1}} < T^n \right. \right.$$

$$\left. \left. \bigcap_{\substack{t_i \\ t_i \neq t_r}} \|\mathbf{b}_{k,M}^{j,t_r}\|_{\mathbf{R}_{j,t_r}^{-1}} \leq \|\mathbf{b}_{k,M}^{j,t_i}\|_{\mathbf{R}_{j,t_i}^{-1}} \right] \right) \quad (36)$$

Note, the landmark from which feature j is extracted is unknown, but the landmark to which feature j is associated is known, which makes the quantification of $P(MA_j)$ easier.

By denoting the landmark that feature j is associated to as t_{j*} (such that if $t_{j*} = t_j$, then feature j is not mis-associated), the risk of mis-association for feature j will be quantified by the probability of associating a non-corresponding feature to landmark t_{j*}:

$$P(MA_j) \leq P\left(\bigcup_{\substack{i^*=1 \\ i^* \neq j^*}}^{n_{k,M}^F} \left[\|\mathbf{b}_{k,M}^{i^*,t_{j*}}\|_{\mathbf{R}_{i^*,t_{j*}}^{-1}} < T^n \right. \right.$$

$$\left. \left. \bigcap_{\substack{t_{r*} \\ t_{r*} \neq t_{j*}}} \|\mathbf{b}_{k,M}^{i^*,t_{j*}}\|_{\mathbf{R}_{i^*,t_{j*}}^{-1}} \leq \|\mathbf{b}_{k,M}^{i^*,t_{r*}}\|_{\mathbf{R}_{i^*,t_{r*}}^{-1}} \right] \right) \quad (37)$$

where i^* refers to the feature extracted from the ith associated landmark, and $n_{k,M}^F$ is the number of associated landmarks in the time window. Note that this interpretation of the probability of mis-association for feature j, is an upper-bound (not exact) because it is possible for more than one feature to be associated to landmark t_{j*} simultaneously (other than the jth feature). The risk of mis-association for feature j will be further upper-bounded by assuming that the mis-association event would occur whenever a non-corresponding feature lies in the validation region of landmark t_{j*} and then by replacing the union by the sum of the individual probabilities:

$$P(MA_j) \leq P\left(\bigcup_{\substack{i^*=1 \\ i^* \neq j^*}}^{n_{k,M}^F} \|\mathbf{b}_{k,M}^{i^*,t_{j*}}\|_{\mathbf{R}_{i^*,t_{j*}}^{-1}} < T^n \right)$$

$$\leq \sum_{\substack{i^*=1 \\ i^* \neq j^*}}^{n_{k,M}^F} P\left(\|\mathbf{b}_{k,M}^{i^*,t_{j*}}\|_{\mathbf{R}_{i^*,t_{j*}}^{-1}} < T^n \right) \quad (38)$$

Using (12), mis-association risk will be expanded by substituting the definition of the individual residual vector, $\mathbf{b}_{k,M}^{i,t_{j*}}$:

$$P(MA_j) \leq \sum_{\substack{i^*=1 \\ i^* \neq j^*}}^{n_{k,M}^F} P\left(\|\mathbf{V}_{i^*}^{-\frac{1}{2}} \left(\mathbf{y}_{k,M}^{t_{i*},t_{j*}} + \mathbf{v}_{i^*} \right) - \right.$$

$$\left. \mathbf{A}_{k,M}^{t_j^*}\mathbf{\Lambda}_{k,M}^{-1}\mathbf{A}_{k,M}^T\mathbf{V}^{-\frac{1}{2}}(\mathbf{v}+\mathbf{f}) \|_{\mathbf{R}_{i^*,t_{j*}}^{-1}} < T^n \right) \quad (39)$$

Now, the probability of mis-association will be upper-bounded

by utilizing this inequality, $\|\mathbf{a}+\mathbf{b}\| \geq \|\mathbf{a}\| - \|\mathbf{b}\|$:

$$P(MA_j) \leq \sum_{\substack{i^*=1 \\ i^* \neq j^*}}^{n_{k,M}^F} P\left(\|\mathbf{V}_{i^*}^{-\frac{1}{2}}\mathbf{v}_{i^*} \right.$$

$$\left. - \mathbf{A}_{k,M}^{t_j^*}\mathbf{\Lambda}_{k,M}^{-1}\mathbf{A}_{k,M}^T\mathbf{V}^{-\frac{1}{2}}(\mathbf{v}+\mathbf{f})\|_{\mathbf{R}_{i^*,t_{j*}}^{-1}} \right.$$

$$\left. > \|\mathbf{V}_{i^*}^{-\frac{1}{2}}\mathbf{y}_{k,M}^{t_{i*},t_{j*}}\|_{\mathbf{R}_{i^*,t_{j*}}^{-1}} - T^n \right) \quad (40)$$

where $\|\mathbf{V}_{i^*}^{-\frac{1}{2}}\mathbf{y}_{k,M}^{t_{i*},t_{j*}}\|_{\mathbf{R}_{i^*,t_{j*}}^{-1}}$ is a measure of separation between landmark t_{i^*} and landmark t_{j^*} in the measurement space, which are known. Notice that all of the unknown terms are combined in the left hand side, whereas the known terms are lumped in the right hand side. From (13), $\left(\mathbf{E}_{i^*} - \mathbf{A}_{k,M}^{t_j^*}\mathbf{\Lambda}_{k,M}^{-1}\mathbf{A}_{k,M}^T \right)\mathbf{V}^{-\frac{1}{2}}\mathbf{v}$ follows a Gaussian distribution with $\mathbf{R}_{i^*,t_{j*}}$ as the covariance matrix. Thus, the risk of of mis-association for feature j can be expressed as:

$$P(MA_j) \leq \sum_{\substack{i^*=1 \\ i^* \neq j^*}}^{n_{k,M}^F} \left(1 - X_{m_F,\lambda_{i^*,t_{j*}}}^2 \left[\|\mathbf{V}_{i^*}^{-\frac{1}{2}}\mathbf{y}_{k,M}^{t_{i*},t_{j*}}\|_{\mathbf{R}_{i^*,t_{j*}}^{-1}} - T^n \right]^2 \right)$$

$$\leq n_{k,M}^F - 1 - \sum_{\substack{i^*=1 \\ i^* \neq j^*}}^{n_{k,M}^F} \left(X_{m_F,\lambda_k^{i^*,t_{j*}}}^2 \left[\|\mathbf{V}_{i^*}^{-\frac{1}{2}}\mathbf{y}_{k,M}^{t_{i*},t_{j*}}\|_{\mathbf{R}_{i^*,t_{j*}}^{-1}} - T^n \right]^2 \right)$$

$$(41)$$

where m_F is the number of independent measurements in each feature and $\lambda_k^{i^*,t_{j*}}$ is the non-centrality parameter, defined as:

$$\lambda_k^{i^*,t_{j*}} = \mathbf{f}^T\mathbf{V}^{-\frac{1}{2}}\mathbf{A}_{k,M}\mathbf{\Lambda}_{k,M}^{-1}\mathbf{A}_{k,M}^{t_j^*\,T}\mathbf{R}_{i^*,t_{j*}}^{-1}\mathbf{A}_{k,M}^{t_j^*}\mathbf{\Lambda}_{k,M}^{-1}\mathbf{A}_{k,M}^T\mathbf{V}^{-\frac{1}{2}}\mathbf{f} \quad (42)$$

Note that $\lambda_k^{i^*,t_{j*}}$ is a function of measurement faults and so it is the only unknown quantity in the mis-association risk bound of the jth feature.

To address this, the non-detection event, $q_k \leq T_k$, at the current time will be assumed to have occurred and will be utilized to upper-bound the non-centrality parameter, $\lambda_k^{i^*,t_{j*}}$. This assumption is valid because the evaluation of integrity risk at the current time is not needed if the detector triggers an alarm. However, since the detector's non-centrality parameter, λ_k, is different from $\lambda_k^{i^*,t_{j*}}$, the linear proportionality factor between them, $\Gamma_{i^*,t_{j*}}$, is given as:

$$\lambda_k^{i^*,t_{j*}} = \Gamma_k^{i^*,t_{j*}}\lambda_k \quad (43)$$

where $\Gamma_k^{i^*,t_{j*}}$ is:

$$\Gamma_k^{i^*,t_{j*}} = \frac{\lambda_k^{i^*,t_{j*}}}{\lambda_k}$$

$$= \frac{\mathbf{f}^T\mathbf{V}^{-\frac{1}{2}}\mathbf{A}_{k,M}\mathbf{\Lambda}_{k,M}^{-1}\mathbf{A}_{k,M}^{t_j^*\,T}\mathbf{R}_{i^*,t_{j*}}^{-1}\mathbf{A}_{k,M}^{t_j^*}\mathbf{\Lambda}_{k,M}^{-1}\mathbf{A}_{k,M}^T\mathbf{V}^{-\frac{1}{2}}\mathbf{f}}{\mathbf{f}^T\mathbf{V}^{-\frac{1}{2}}\left(\mathbf{I} - \mathbf{A}_{k,M}\mathbf{\Lambda}_{k,M}^{-1}\mathbf{A}_{k,M}^T \right)\mathbf{V}^{-\frac{1}{2}}\mathbf{f}}$$

$$(44)$$

Since $\left(\mathbf{I}-\mathbf{A}_{k,M}\boldsymbol{\Lambda}_{k,M}^{-1}\mathbf{A}_{k,M}^{T}\right)$ is an idempotent rank deficient matrix, the proportionality factor will be quantified for each hypothesis alone, $\Gamma_{k,h}^{i^*,t_{j^*}}$, as follows:

$$\Gamma_{k,h}^{i^*,t_{j^*}} = \frac{\mathbf{f}^T\mathbf{V}^{-\frac{1}{2}}\mathbf{A}_{k,M}\boldsymbol{\Lambda}_{k,M}^{-1}{\mathbf{A}_{k,M}^{t_{j^*}}}^{T}\mathbf{R}_{i^*,t_{j^*}}^{-1}\mathbf{A}_{k,M}^{t_{j^*}}\boldsymbol{\Lambda}_{k,M}^{-1}\mathbf{A}_{k,M}^{T}\mathbf{V}^{-\frac{1}{2}}\mathbf{f}}{\mathbf{f}^T\mathbf{V}^{-\frac{1}{2}}\left(\mathbf{I}-\mathbf{A}_{k,M}\boldsymbol{\Lambda}_{k,M}^{-1}\mathbf{A}_{k,M}^{T}\right)\mathbf{V}^{-\frac{1}{2}}\mathbf{f}}$$

$$= \frac{\mathbf{f}^T\mathbf{V}^{-\frac{1}{2}}\mathbf{F}_h^T\mathbf{F}_h\mathbf{A}_{k,M}\boldsymbol{\Lambda}_{k,M}^{-1}{\mathbf{A}_{k,M}^{t_{j^*}}}^{T}\mathbf{R}_{i^*,t_{j^*}}^{-1}\mathbf{A}_{k,M}^{t_{j^*}}\boldsymbol{\Lambda}_{k,M}^{-1}\mathbf{A}_{k,M}^{T}\mathbf{F}_h^T\mathbf{F}_h\mathbf{V}^{-\frac{1}{2}}\mathbf{f}}{\mathbf{f}^T\mathbf{V}^{-\frac{1}{2}}\mathbf{F}_h^T\mathbf{F}_h\left(\mathbf{I}-\mathbf{A}_{k,M}\boldsymbol{\Lambda}_{k,M}^{-1}\mathbf{A}_{k,M}^{T}\right)\mathbf{F}_h^T\mathbf{F}_h\mathbf{V}^{-\frac{1}{2}}\mathbf{f}}$$

$$\tag{45}$$

By defining $\mathbf{N}_{k,h} = \mathbf{F}_h\left(\mathbf{I}-\mathbf{A}_{k,M}\boldsymbol{\Lambda}_{k,M}^{-1}\mathbf{A}_{k,M}^{T}\right)\mathbf{F}_h^T$, and $\mathbf{f}_h = \mathbf{N}_h^{1/2}\mathbf{F}_h\mathbf{V}^{-\frac{1}{2}}\mathbf{f}$ as the vector of measurement faults in the faulted measurements of the hth hypothesis, the proportionality factor for the hth hypothesis can be rewritten as:

$$\Gamma_{k,h}^{i^*,t_{j^*}}$$
$$= \frac{\mathbf{f}_h^T\mathbf{N}_{k,h}^{-\frac{1}{2}}\mathbf{F}_h\mathbf{A}_{k,M}\boldsymbol{\Lambda}_{k,M}^{-1}{\mathbf{A}_{k,M}^{t_{j^*}}}^{T}\mathbf{R}_{i^*,t_{j^*}}^{-1}\mathbf{A}_{k,M}^{t_{j^*}}\boldsymbol{\Lambda}_{k,M}^{-1}\mathbf{A}_{k,M}^{T}\mathbf{F}_h^T\mathbf{N}_{k,h}^{-\frac{1}{2}}\mathbf{f}_h}{\mathbf{f}_h^T\mathbf{f}_h}$$
$$\leq \beta\left(\mathbf{N}_{k,h}^{-\frac{1}{2}}\mathbf{F}_h\mathbf{A}_{k,M}\boldsymbol{\Lambda}_{k,M}^{-1}{\mathbf{A}_{k,M}^{t_{j^*}}}^{T}\mathbf{R}_{i^*,t_{j^*}}^{-1}\mathbf{A}_{k,M}^{t_{j^*}}\boldsymbol{\Lambda}_{k,M}^{-1}\mathbf{A}_{k,M}^{T}\mathbf{F}_h^T\mathbf{N}_{k,h}^{-\frac{1}{2}}\right)$$
$$\tag{46}$$

where $\beta\left(\cdot\right)$ is a function that returns the maximum eigenvalue of the input matrix.

Given the upper-bound on the proportionality factor for each hypothesis among $h \not\in > n_{max}$, the upper-bounded proportionality factor, $\breve{\Gamma}_k^{i^*,t_{j^*}}$, will be defined as follows:

$$\Gamma_k^{i^*,t_{j^*}} \leq \breve{\Gamma}_k^{i^*,t_{j^*}} = \max_{\substack{h=0 \\ h\not\in>n_{max}}}^{n_H} \Gamma_{k,h}^{i^*,t_{j^*}} \tag{47}$$

After bounding $\Gamma_k^{i^*,t_{j^*}}$, the only unknown in the upper-bound on the non-centrality parameter, $\lambda_k^{i^*,t_{j^*}}$, is the detector's non-centrality parameter, λ_k. [30] demonstrated that the non-detection event can be utilized to upper-bound the non-centrality parameter of any chi-squared based fault detector (using confidence intervals), such that the probability of failure for the bound is less than I_{NC}:

$$\lambda_k \leq \breve{\lambda}_k = \left(\sqrt{T_k} + \sqrt{X_{n_{k,M}-(M+1)m}^{-2}[1-I_{NC}]}\right)^2 \tag{48}$$

where $\breve{\lambda}_k$ is the upper-bound on the non-centrality parameter of the chi-squared fault detector, λ_k, and $P\left(\breve{\lambda}_k < \lambda_k\right) \leq I_{NC}$.

Using the bounds on the proportionality factor, $\breve{\Gamma}_k^{i^*,t_{j^*}}$, and the the detector's non-centrality parameter, $\breve{\lambda}_k$, the non-centrality parameter, $\lambda_k^{i^*,t_{j^*}}$, defined in (43), will be upper-bounded as follows:

$$\lambda_k^{i^*,t_{j^*}} \leq \breve{\lambda}_k^{i^*,t_{j^*}} = \breve{\Gamma}_k^{i^*,t_{j^*}}\breve{\lambda}_k \tag{49}$$

Now, the bound on the non-centrality parameter, $\breve{\lambda}_k^{i^*,t_{j^*}}$, will be substituted back into the bound on the probability of mis-association for the jth feature, $P(MA_j)$, defined in (41):

$$P\left(MA_j\right) \leq I_{NC} + P\left(MA_j \mid \lambda_k \leq \breve{\lambda}_k\right)\left(1-I_{NC}\right) \tag{50}$$

Algorithm 1 Fixed-lag smoothing integrity monitoring

1: Estimate robot pose, $\hat{\mathbf{x}}_{k,M}$ within the window using (1).
2: Evaluate the detector, and its threshold using (16), (24).
3: **if** the alarm is not triggered **then**
4:      Evaluate the bound on the detector's non-centrality parameter, $\breve{\lambda}_k$, using (48), given a predefined I_{NC}.
5:      **for** every associated feature j **do**
6:          Evaluate $\breve{\Gamma}_k^{i^*,t_{j^*}}$, followed by $\breve{\lambda}_k^{i^*,t_{j^*}}$, $\forall i^* \neq j^*$, using (46), (47), (49), given a specific n_{max}.
7:          Evaluate $P(MA_j)$ using (51),(50).
8:          Evaluate the upper-bound on the failure probability of feature j, P_j, using (35).
9:          Evaluate $I_{>n_{max}}$ using (33), given a specific n_{max}.
10:          **for** every hypothesis H_h, $\forall h \in 0,...,n_H$, $h \not\in > n_{max}$ **do**
11:              Evaluate the probability of the hth hypothesis, $P(H_h)$, using (31).
12:              Evaluate the worst-case fault direction, $\mathbf{f}_h^{dir}$, for the hth hypothesis using (29).
13:              Quantify the conditional integrity risk given the hth hypothesis, $P(HMI_k|H_h)$, using (30).
14:          Evaluate the integrity risk, $P(HMI_k)$, using (32).

---

where the conditional probability of mis-association given that the upper-bound on the detector's non-centrality parameter is valid:

$$P\left(MA_j \mid \lambda_k \leq \breve{\lambda}_k\right) \leq$$
$$n_{k,M}^F - 1 - \sum_{\substack{i^*=1 \\ i^* \neq j^*}}^{n_{k,M}^F}\left(X_{m_F,\breve{\lambda}_k^{i^*,t_{j^*}}}^2\left[\|\mathbf{V}_{i^*}^{-\frac{1}{2}}\mathbf{y}_{k,M}^{t_{i^*},t_{j^*}}\|_{\mathbf{R}_{i^*,t_{j^*}}^{-1}} - T^n\right]^2\right)$$
$$\tag{51}$$

This section quantified the probability of data association failure for features extracted from lidar or camera measurements, thus allowing integrity to be monitored using (32). Algorithm 1 summarizes the main bounds needed to monitor localization safety. In the next section, simulation and experimental results will be used to demonstrate and assess the proposed integrity risk bound in practical scenarios.

VII. Results

This section quantifies mobile robot localization safety for a fixed lag smoothing estimator while accounting for the risk of data association errors (mis-association and unmapped association events) in both simulation and experimentation. Simulation results assess the impact of mis-association and unmapped association events on the state-of-interest estimate error and on the the fault detector as well as the impact of different landmark densities in the map on mobile robot localization safety. Experimental results demonstrate the performance of the proposed integrity risk bound in quantifying fixed lag smoothing-based localization safety in a landmark-rich, urban environment.

A. Simulation Results

The simulations depict a mobile robot modeled using a constant-speed bicycle-model navigating through predefined
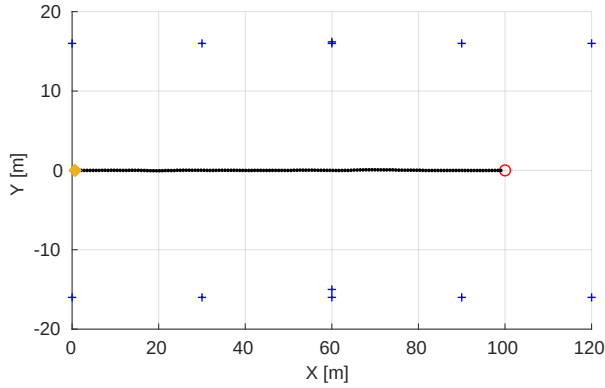
312

Fig. 1. Estimated mobile robot trajectory while traversing a pre-mapped environment. Blue plus-signs represent landmarks, the yellow cross-sign is the starting location, and the red circle is the end.

TABLE I
SIMULATION PARAMETERS

Velocity	$25\,\mathrm{km\,h^{-1}}$	$\sigma_{velocity}$	$0.1\,\mathrm{m\,s^{-1}}$
Time step	$0.1\,\mathrm{s}$	σ_{gyro}	$2\,^{\circ}\,\mathrm{s^{-1}}$
Sensor range	$25\,\mathrm{m}$	σ_{lidar}	$0.2\,\mathrm{m}$
Alert limit	$1.0\,\mathrm{m}$	$\sigma_{steering\ angle}$	$0.4\,^{\circ}$
I_{NC}	10^{-8}	I_{FA}	10^{-5}
P_{UA}	10^{-9}	n_{max}	2

way-points in a landmark-rich environment (see Fig. 1). Steering angle as well as linear and angular velocities comprise the robot's relative measurements. Absolute measurements are composed of range and bearing to mapped landmarks. We assume that relative measurements are fault free, and that absolute measurements can be faulted, either from unmapped association or mis-association events. To maintain acceptable computational requirements, the time window is continuously resized to include the minimum number of landmark detections above 15, which has previously been shown to be a reasonable compromise between computation time and tightness of the integrity risk bound [32]. The simulation parameters are shown in Table I.

The simulation results have been divided into two parts. The first simulation investigates the superiority of the proposed integrity monitoring methodology over the common 3σ covariance bound when accounting for measurement faults. The second simulation shows the trade-off between landmark density and localization safety.

To assess the effectiveness of the proposed method, the landmark map has been configured so that all landmarks are well-separated except for two, one on each side of the path at $X = 60\,\mathrm{m}$ (see Fig. 1). The estimate error in the state-

TABLE II
OBSERVATIONS FROM THE SIMULATION

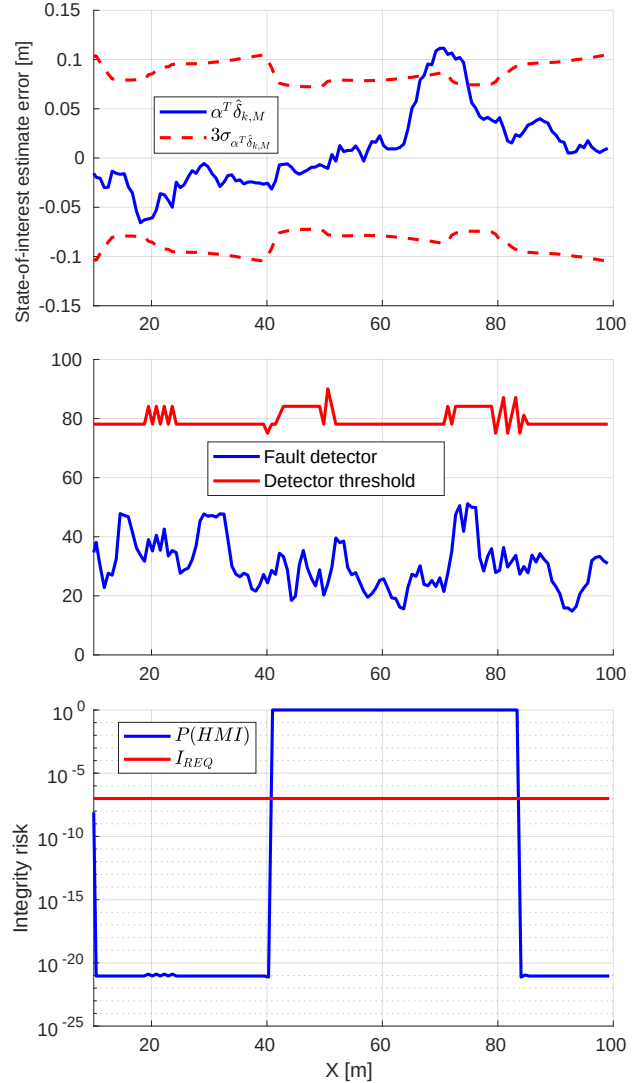|	Landmarks Density [m^{-2}]		
	1e-3	2.5e-3	6.5e-3
Avg. time window size (epochs)	10.6	4.9	3.1
Avg. # of landmarks in the window	15.6	17.0	24.7

Fig. 2. The top figure shows the estimate error and the 3σ covariance bounds in the state-of-interest (robot's lateral direction) versus robot's longitudinal position. Moreover, the middle figure presents the chi-squared fault detector (blue) and the associated threshold (red) versus robot's longitudinal position, whereas the bottom figure shows the localization integrity risk (blue) and the predefined safety requirement (red) versus robot's longitudinal position.

of-interest (lateral error) and the associated 3σ covariance bounds versus the robot's position in the longitudinal direction are shown in the top of Fig. 2. The middle section of Fig. 2 presents the chi-squared fault detector and the associated threshold as a function of robot's position in the X direction. The localization integrity risk and the predefined safety requirement (chosen to be $1e^{-7}$ based on the FAA requirement on extremely hazardous remote events, [37]) versus the robot's longitudinal position are shown in the bottom part of Fig. 2.

The integrity risk approaches one when the robot is between $X = 60$ and $85\,\mathrm{m}$ while the detector is not triggered and the state-of-interest estimate error is not bounded by the 3σ covariance bounds. This is because, in addition to the lack of sufficient redundancy, there are two close landmarks on each side of the road at $X = 60\mathrm{m}$, which results in a high risk of having undetected large positioning errors due to the
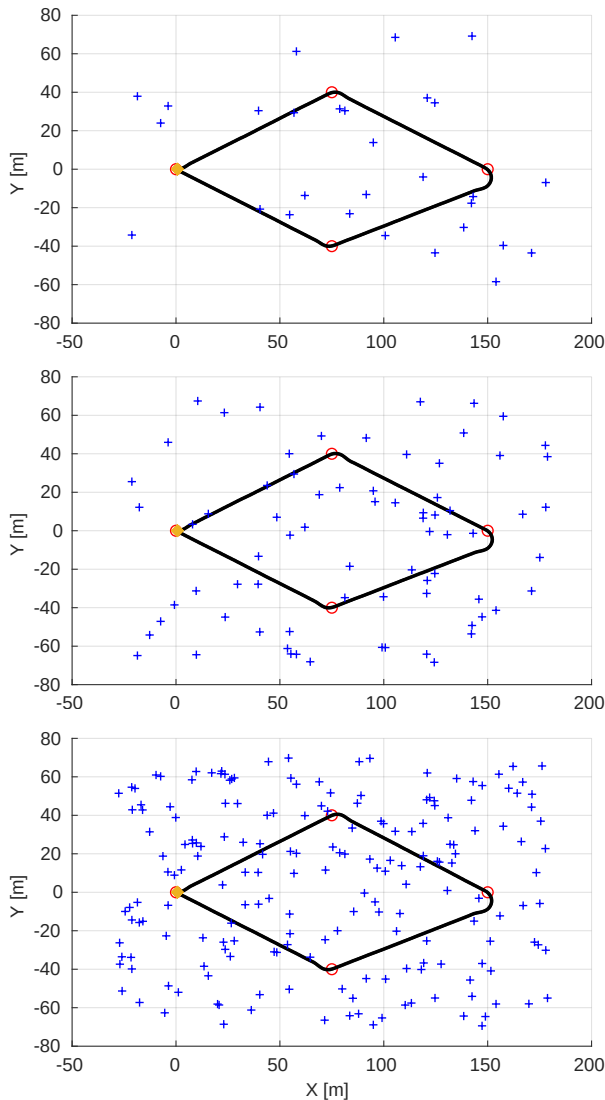
Fig. 3. Estimated robot trajectory while navigating through a set of way-points in each of the three randomly generated landmark maps ($1e^{-3}$ (top), $2.5e^{-3}$ (middle), and $6.5e^{-3}$ (bottom) landmarks/m^2). Blue plus-signs refer to landmarks, the yellow cross-sign is the robot's starting location, and the red circle represents the set of way-points.
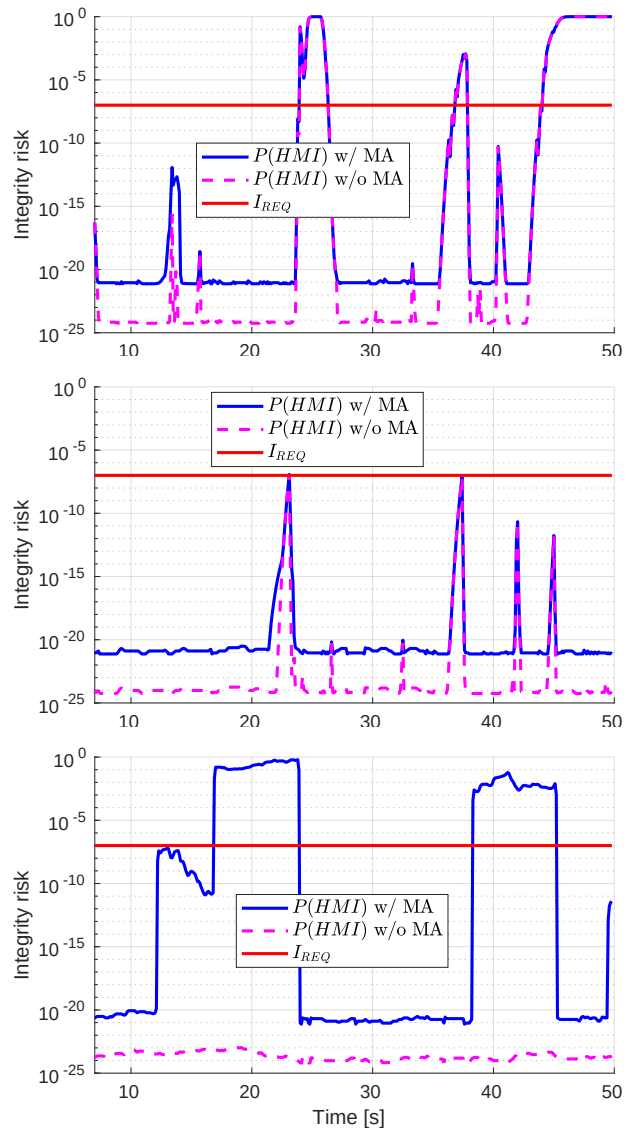

Fig. 4. The proposed integrity risk that accounts for the risk of misassociation (blue), the integrity risk that ignores the risk of misassociation (pink) and the predefined safety requirement (red) versus time for the three different landmarks densities 1e-3, 2.5e-3 6.5e-3 landmarks/m^2 (top, middle, bottom). Too few landmarks (top) results in an integrity risk that peaks above the integrity requirement because a minimum number of landmarks is needed to guarantee integrity. Too many landmarks (bottom) results integrity risk that peaks above the integrity requirement because more landmarks results in a higher chance of misassociations.

mis-association event. In landmark-based fixed lag smoothing localization, redundancy is influenced by the number of landmark detections in the preceding time window and the percentage of them that are close to the most recent state in the time window. Therefore, unlike the 3σ covariance bounds, the proposed integrity risk metric provides a sufficient measure of localization safety.

To study the relationship between landmark density and localization safety, three landmark maps have been generated randomly with different densities (see Fig. 3 and Table II). Note, the size of the preceding time window decreases as landmark density increases to maintain the smallest number of landmark detections in the window above 15. For each landmark density, the simulated robot navigates through the way-points in the corresponding landmark-rich environment, and the corresponding integrity risk is evaluated twice (with

and without accounting for the risk of misassociation), see Fig. 4.

When landmark density is relatively low (see Fig. 3, top), the integrity risk exceeds the safety requirement due to the lack of sufficient redundancy. This results in an availability of 76%, which is the percentage of time integrity risk is below a predefined safety requirement (chosen here to be $I_{REQ} = 10^{-7}$). Moreover, the difference between the proposed integrity risk and the integrity risk that ignores the risk of misassociation is negligible due to the relatively large distance (in the measurement space) among the landmarks in the map. Last, when the integrity risk is low, the difference between the integrity risk

Fig. 5. The test setup used for the experiment. The sensor suite consists of STIM-300 tactical-grade IMU, two Velodyne VLP-16 lidars, one Ouster-64 lidar and Novatel SPAN-CPT DGPS attached to a roof-rack of a vehicle. For this experiment only the STIM-300 and Ouster lidar were used. Columns, tree trunks, and lamp posts are used as landmarks for localization.

with and without accounting for the misassociation probability is due to the allocated risk for the non-centrality parameter, I_{NC}.

Note that the integrity risk after 45 s approaches one, although the time window is continuously resized to include a minimum of 15 landmark detections. This is because, after 45 s there are no landmarks in the robot's field of view, which results in a large increase in the size of the time window. Therefore, the proportion of landmark detections that are close to the most-recent state in the time window reduces, and accordingly the uncertainty in the state-of-interest estimate increases.

On the other hand, when the landmark density is moderate (see Fig. 3, middle), the integrity risk stays below the safety requirement along the trajectory, yielding 100% availability. This is because sufficient redundancy exists throughout the trajectory while all of the landmarks are well-separated. Similar to the low landmark density case, the difference between the proposed integrity risk and the integrity risk that ignores the risk of misassociation is negligible due to the relatively moderate distance (in the measurement space) among the landmarks.

Finally, when landmark density is relatively high (see Fig. 3, bottom), the integrity risk surpasses the safety requirement, resulting in a 69% availability. Although there is sufficient redundancy, high inter-landmark proximity results in a high risk of having undetected mis-association events that subsequently lead to large estimate errors. Unlike the low and moderate landmark density cases, the difference between the proposed integrity risk and the integrity risk that ignores the risk of misassociation is significant due to the relatively small distance (in the measurement space) among the landmarks. This example provides a clear rationale for the necessity to account for the risk of misassociation and demonstrates that in fixed-lag smoothing, high localization safety can be achieved if landmarks are both well-separated and have sufficient re-

Fig. 6. The transect used for experiments consists of S. State Street from 31st to 33rd in Chicago, IL.

TABLE III
EXPERIMENT PARAMETERS

$PSD_{AccelNoise}$	$0.002 \, \mathrm{m^2/s^5}$	Alert limit	$1.0 \, \mathrm{m}$
$PSD_{GyroNoise}$	$3.05 \times 10^{-6} \, \mathrm{rad^2/s^3}$	σ_{lidar}	$0.3 \, \mathrm{m}$
$PSD_{AccelBias}$	$2.40 \times 10^{-7} \, \mathrm{m^2/s^6}$	$\mathrm{frequency}_{lidar}$	$10 \, \mathrm{Hz}$
$PSD_{GyroBias}$	$2.12 \times 10^{-12} \, \mathrm{rad^2/s^4}$	$\mathrm{frequency}_{IMU}$	$125 \, \mathrm{Hz}$
I_{NC}	10^{-12}	P_{UA}	10^{-9}
I_{FA}	10^{-5}	n_{max}	2

dundancy.

B. Experimental Results

The proposed localization safety method was tested in an urban environment (S. State Street from 31st to 33rd St.) in Chicago, IL USA where GPS signals are denied or degraded due to dense tree coverage and tall buildings lining the street (see Fig. 6). The sensor suite mounted on a vehicle's roof rack (see Fig. 5) consists of a STIM-300 tactical grade inertial measurement unit for relative measurements, and a 64-beam Ouster lidar for range and bearing measurements to lamp posts, columns, and tree trunks that comprise the mapped landmarks. In this experiment, GPS was not utilized because, even when it was available, multi-path errors made the measurements unsuitable.

Table III shows the parameters of the experiment. SLAM was used to build the landmark map prior to the experiments. The state vector is composed of fifteen variables: six for the position and orientation, three for the linear velocities, and six for the accelerometers and gyroscopes biases. The landmark map and the estimated trajectory are shown in Fig. 7. The state-of-interest is the vehicle's lateral position with an alert limit of $1.0 \, \mathrm{m}$. Finally, the preceding time window is continuously resized so that it includes the minimum number of landmark detections above 30.

The number of landmark detections in the preceding time window and the number of landmark detections in the current time versus the distance travelled by the vehicle are presented in Fig. 8. Note that the proportion of landmark detections that are close to the most recent state in the time window is relatively high. This is an indication for the existence of sufficient redundancy.
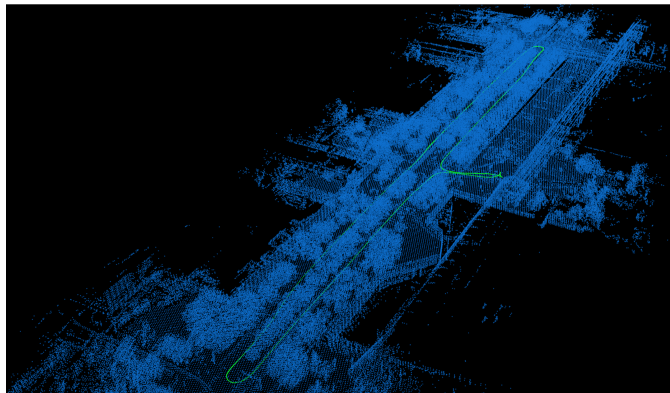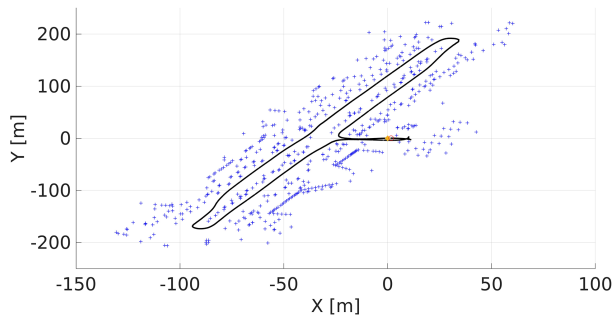
315

Fig. 8. The number of landmark detections in the preceding time window (blue) and current time (red) versus distance travelled.

Fig. 7. (Top) The vehicle's estimated trajectory and landmark map. The yellow dot, at $(0, 0)$, is the vehicle's starting location, the red circle refers to the ending location, and the blue-plus signs represent the mapped landmarks (columns, tree trunks, and lamp posts). (Bottom) The 3D point-cloud generated from the lidar.

Localization integrity risk with and without considering the risk of misassociation versus the distance travelled by the vehicle are shown in Fig. 9. Note that the difference between the proposed integrity risk that accounts for the risk of misassociation and the integrity risk that ignores the risk of misassociation is significant in a large proportion of the trajectory, resulting in 61% availability. Although there exists sufficient redundancy, several landmarks are very close to each other, which results in high risk of undetected misassociation events that cause large estimate error in the state-of-interest.

This scenario provides a strong evidence for the necessity to account for the risk of misassociation and demonstrates that in fixed-lag smoothing, high localization safety can be achieved if the mapped landmarks provide sufficient redundancy and are well-separated.

Fig. 9. The proposed integrity risk that accounts for the risk of misassociation (blue), the integrity risk that ignores the risk of misassociation (pink) and the predefined safety requirement (red) versus distance travelled.

available at *https://github.com/mspenko/RoboticsLab-Integrity-Evaluation*.

VIII. CONCLUSION AND FUTURE WORK

This paper presents a mobile robot localization safety method for landmark-based fixed-lag smoothing estimation that accounts for data association errors. The results show that the risk of misassociation has a significant impact on localization integrity risk if landmark density in the map is high, as well as that robot localization safety is high if the landmarks in the map are well-separated while having enough redundancy. The future work will focus on deriving integrity monitoring techniques for the more challenging Simultaneous Localization And Mapping (SLAM) problem. The computer code utilized to evaluate integrity is
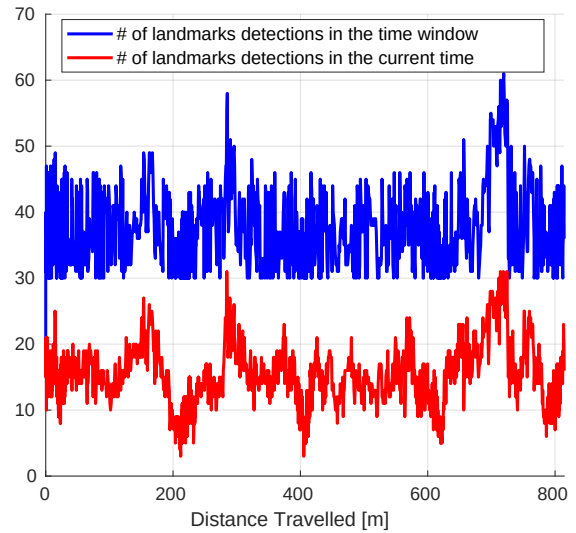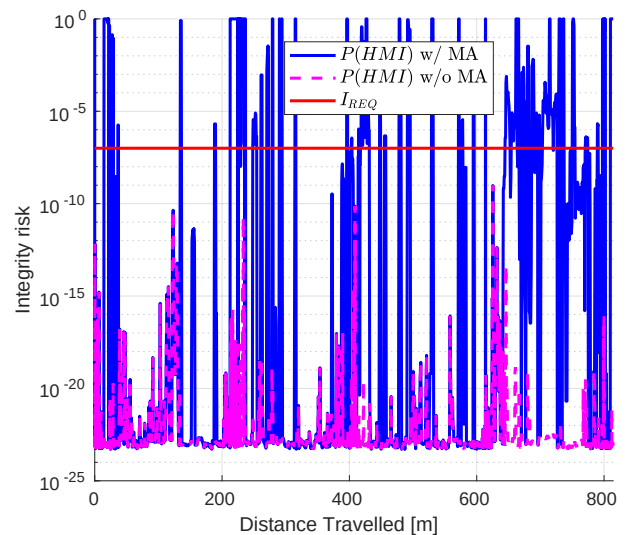
REFERENCES

[1] K. Wiggers, "Waymo's autonomous cars have driven 20 million miles on public roads," Jan 2020. [Online]. Available: https://venturebeat.com/2020/01/06/waymos-autonomous-cars-have-driven-20-million-miles-on-public-roads/

[2] N. Kalra and S. M. Paddock, "Driving to safety: How many miles of driving would it take to demonstrate autonomous vehicle reliability?" *Transportation Research Part A: Policy and Practice*, vol. 94, pp. 182 – 193, 2016. [Online]. Available: http://www.sciencedirect.com/science/article/pii/S0965856416302129

[3] K. Korosec, "Waymo's autonomous vehicles are driving 25,000 miles every day," Jul 2018. [Online]. Available: https://techcrunch.com/2018/07/20/waymos-autonomous-vehicles-are-driving-25000-miles-every-day/

[4] F. Dellaert and M. Kaess, "Factor graphs for robot perception," *Foundations and Trends® in Robotics*, vol. 6, pp. 1–139, 2017.

[5] G. Gallego and D. Scaramuzza, "Accurate angular velocity estimation with an event camera," *IEEE Robotics and Automation Letters*, vol. 2, no. 2, pp. 632–639, April 2017.

[6] R. Dubé, M. G. Gollub, H. Sommer, I. Gilitschenski, R. Siegwart, C. Cadena, and J. Nieto, "Incremental-segment-based localization in 3-d point clouds," *IEEE Robotics and Automation Letters*, vol. 3, no. 3, pp. 1832–1839, July 2018.

[7] M. Hsiao and M. Kaess, "Mh-isam2: Multi-hypothesis isam using bayes tree and hypo-tree," in *2019 International Conference on Robotics and Automation (ICRA)*, May 2019, pp. 1274–1280.

[8] J. Kim and W. Chung, "Robust localization of mobile robots considering reliability of lidar measurements," in *2018 IEEE International Conference on Robotics and Automation (ICRA)*, May 2018, pp. 6491–6496.

[9] S. I. Roumeliotis and I. M. Rekleitis, "Analysis of multirobot localization uncertainty propagation," in *Proceedings 2003 IEEE/RSJ International Conference on Intelligent Robots and Systems (IROS 2003) (Cat. No.03CH37453)*, vol. 2, Oct 2003, pp. 1763–1770 vol.2.

[10] S. Bonnabel, M. Barczyk, and F. Goulette, "On the covariance of icp-based scan-matching techniques," in *2016 American Control Conference (ACC)*, July 2016, pp. 5498–5503.

[11] S. Thrun, W. Burgard, and D. Fox, *Probabilistic robotics*. MIT press, 2005.

[12] N. Othman and H. Ahmad, "The analysis of covariance matrix for kalman filter based slam with intermittent measurement," in *Proceedings of the 2013 International Conference on Systems, Control and Informatics*, 2013.

[13] V. Kadirkamanathan, P. Li, M. H. Jaward, and S. G. Fabri, "Particle filtering-based fault detection in non-linear stochastic systems," *International Journal of Systems Science*, vol. 33, no. 4, pp. 259–265, 2002.

[14] S. Yilmaz, H. E. Kayir, B. Kaleci, and O. Parlaktuna, "Mobile robot localization via outlier rejection in sonar range sensor data," in *2011 7th International Conference on Electrical and Electronics Engineering (ELECO)*, Dec 2011, pp. II–434–II–438.

[15] A. Das and S. L. Waslander, "Outlier rejection for visual odometry using parity space methods," in *2014 IEEE International Conference on Robotics and Automation (ICRA)*, May 2014, pp. 3613–3618.

[16] R. Kelly and J. Davis, "Required navigation performance (rnp) for precision approach and landing with gnss application," *Navigation*, 1994.

[17] B. W. Parkinson and P. Axelrad, "Autonomous GPS Integrity Monitoring Using the Pseudorange Residual," *Navigation*, vol. 35, no. 2, pp. 225–274, 1988.

[18] J. Blanch, T. Walker, P. Enge, Y. Lee, B. Pervan, M. Rippl, A. Spletter, and V. Kropp, "Baseline advanced raim user algorithm and possible improvements," *IEEE Transactions on Aerospace and Electronic Systems*, vol. 51, no. 1, pp. 713–732, 2015.

[19] C. Tanıl, S. Khanafseh, M. Joerger, and B. Pervan, "Sequential integrity monitoring for kalman filter innovations-based detectors," in *31st International Technical Meeting of the Satellite Division of the Institute of Navigation, ION GNSS+ 2018*. Institute of Navigation, 2018, pp. 2440–2455.

[20] A. V. Kanhere and G. X. Gao, "Integrity for gps/lidar fusion utilizing a raim framework," in *31st International Technical Meeting of the Satellite Division of the Institute of Navigation, ION GNSS*, 2018, pp. 3145–3155.

[21] C. Li and S. L. Waslander, "Visual measurement integrity monitoring for uav localization," in *2019 IEEE International Symposium on Safety, Security, and Rescue Robotics (SSRR)*, Sep. 2019, pp. 22–29.

[22] M. Joerger, M. Jamoom, M. Spenko, and B. Pervan, "Integrity of laser-based feature extraction and data association," in *2016 IEEE/ION Position, Location and Navigation Symposium (PLANS)*, April 2016, pp. 557–571.

[23] G. Duenas Arana, M. Joerger, and M. Spenko, "Local nearest neighbor integrity risk evaluation for robot navigation," in *2018 IEEE International Conference on Robotics and Automation (ICRA)*, May 2018, pp. 2328–2333.

[24] M. Joerger, G. D. Arana, M. Spenko, and B. Pervan, "Landmark data selection and unmapped obstacle detection in lidar-based navigation," in *30th International Technical Meeting of the Satellite Division of the Institute of Navigation, ION GNSS 2017*. Institute of Navigation, 2017, pp. 1886–1903.

[25] M. Joerger, G. Duenas Arana, M. Spenko, and B. Pervan, "A new approach to unwanted-object detection in gnss/lidar-based navigation," *Sensors*, vol. 18, no. 8, p. 2740, 2018.

[26] A. Hassani, M. Joerger, G. Duenas Arana, and M. Spenko, "Lidar data association risk reduction using tight integration with ins," in *31nd International Technical Meeting of the Satellite Division of the Institute of Navigation, ION GNSS+ 2018*. Institute of Navigation, pp. 2467–2483.

[27] O. A. Hafez, G. D. Arana, and M. Spenko, "Integrity risk-based model predictive control for mobile robots," in *2019 International Conference on Robotics and Automation (ICRA)*, May 2019, pp. 5793–5799.

[28] G. D. Arana, M. Joerger, and M. Spenko, "Efficient integrity monitoring for kf-based localization," in *2019 International Conference on Robotics and Automation (ICRA)*, May 2019, pp. 6374–6380.

[29] G. D. Arana, O. A. Hafez, M. Joerger, and M. Spenko, "Recursive integrity monitoring for mobile robot localization safety," in *2019 International Conference on Robotics and Automation (ICRA)*, May 2019, pp. 305–311.

[30] G. D. Arana, O. A. Hafez, M. Joerger, and M. Spenko, "Integrity monitoring for kalman filter-based localization," *IJRR (submitted)*, 2020.

[31] G. D. Arana, O. A. Hafez, M. Joerger, and M. Spenko, "Localization safety verification for autonomous robots," in *IROS (submitted)*, 2020.

[32] O. A. Hafez, G. D. Arana, M. Joerger, and M. Spenko, "Quantifying robot localization safety: A new integrity monitoring method for fixed-lag smoothing," *IEEE Robotics and Automation Letters*, vol. 5, no. 2, pp. 3181–3188, 2020.

[33] A. Bryson and D. Johansen, "Linear filtering for time-varying systems using measurements containing colored noise," *IEEE Transactions on Automatic Control*, vol. 10, no. 1, pp. 4–10, 1965.

[34] R. Kümmerle, G. Grisetti, H. Strasdat, K. Konolige, and W. Burgard, "G2o: A general framework for graph optimization," in *2011 IEEE International Conference on Robotics and Automation*, May 2011, pp. 3607–3613.

[35] M. Joerger, F.-C. Chan, and B. Pervan, "Solution separation versus residual-based raim," *NAVIGATION: Journal of the Institute of Navigation*, vol. 61, no. 4, pp. 273–291, 2014.

[36] J. Blanch, T. Walter, P. Enge, Y. Lee, B. Pervan, M. Rippl, and A. Spletter, "Advanced raim user algorithm description: integrity support message processing, fault detection, exclusion, and protection level calculation," in *Proceedings of the 25th International Technical Meeting of The Satellite Division of the Institute of Navigation (ION GNSS 2012)*, 2012, pp. 2828–2849.

[37] T. G. Reid, S. E. Houts, R. Cammarata, G. Mills, S. Agarwal, A. Vora, and G. Pandey, "Localization requirements for autonomous vehicles," *arXiv preprint arXiv:1906.01061*, 2019.